Solar Phys (2013) 286:493–507
DOI 10.1007/s11207-013-0276-x

Interpreting Solar EUV Wave Observations from Different Viewing Angles Using an MHD Model

S. Hoilijoki · J. Pomoell · R. Vainio · M. Palmroth · H.E.J. Koskinen

Received: 1 October 2012 / Accepted: 7 March 2013 / Published online: 10 April 2013
© Springer Science+Business Media Dordrecht 2013

Abstract We study the effect of projection and line-of-sight integration on the interpretation of the morphology and kinematics of EUV waves. We have performed a three-dimensional magnetohydrodynamic simulation of a coronal mass ejection (CME) erupting in an environment that mimics the low solar corona and calculated the resulting emission measure of the event from five different viewing angles. Our study provides more quantitative information about the impact of the viewing angle and projection effect on the properties of EUV waves than previous studies on the subject.

Analyzing the emission measure of the lower corona reveals wave-like increases that move away from the eruption site, which we interpret as EUV waves. Behind the EUV wave front we can recognize coronal dimming regions. A comparison of the emission measure and calculated density supports the view that EUV waves are true waves. Our results show that the origin of the observed EUV wave is height-dependent, which means that the measured speed and the morphology depend on the viewing direction. Consequently, care should be taken when EUV observations are used to infer the true propagation speeds of EUV wave fronts.

Keywords Coronal mass ejection · Initiation and propagation · Waves, propagation · Magnetohydrodynamics · Plasma physics

1. Introduction

During the very first coronal mass ejection (CME) watch campaign of the *Solar and Heliospheric Observatory* (SOHO), images of coronal large-scale wave-like disturbances trav-

S. Hoilijoki (✉) · M. Palmroth · H.E.J. Koskinen
Finnish Meteorological Institute, Helsinki, Finland
e-mail: sanni.hoilijoki@fmi.fi

S. Hoilijoki · J. Pomoell · R. Vainio · H.E.J. Koskinen
Department of Physics, University of Helsinki, Helsinki, Finland

J. Pomoell
Centre for Plasma-Astrophysics, Department of Mathematics, KU Leuven, Leuven, Belgium

eling over significant fractions of the solar disk were captured by the *Extreme-ultraviolet Imaging Telescope* (EIT) (Moses *et al.*, 1997). The first detailed reports (Thompson *et al.*, 1998, 1999) characterized the EUV wave phenomenon as a large, bright diffuse wave that propagates across the solar disk quasi-radially away from the eruption site at a speed of a few hundred $\mathrm{km\,s^{-1}}$ in a non-homogeneous fashion, being most pronounced in quiet-Sun regions and less observable near strong magnetic features. Indeed, because of this, it was immediately proposed that the EUV wave could be a signature of the long-sought coronal fast-mode wave predicted by Uchida's model of Moreton waves (Uchida, 1968).

Despite the wealth of observational data that have been accumulated for more than 15 years, the nature of EUV waves remains a matter of debate. Contesting the wave picture, several alternative so-called pseudo-wave interpretations of the observations have been proposed in which the disturbance is not a wave at all, but instead a signature related to the expansion of the eruption complex and its interaction with the surroundings. More recently, a hybrid interpretation suggesting that both wave and non-wave components can be present simultaneously has gained favor (see, *e.g.*, Patsourakos and Vourlidas, 2012). In-depth discussions of the characteristics of EUV waves and the various suggested models have been provided by, *e.g.*, Warmuth (2007), Vršnak and Cliver (2008), Wills-Davey and Attrill (2009), Warmuth (2010), Gallagher and Long (2011), Zhukov (2011), Warmuth (2011), Chen (2011), and Patsourakos and Vourlidas (2012).

With the next generation of space-based observatories, *e.g.*, *Solar TErrestrial RElations Observatory* (STEREO) and *Solar Dynamics Observatory* (SDO), now operational, new high-cadence multi-viewpoint observations have become available that largely rectifying the shortcomings of the EIT in studies of coronal phenomena such as EUV waves. Yet, uncovering clues of the nature of EUV waves from the observational data remains a non-trivial task. As case studies, Dai *et al.* (2012) and Kienreich *et al.* (2012) analyzed three wave events that occurred on 27 January 2011. One the one hand, Kienreich *et al.* (2012) found evidence that the three homologous EUV waves were reflected from the southern polar coronal hole with the reflected waves obeying the Huygens–Fresnel principle, thereby supporting a wave interpretation. On the other hand, Dai *et al.* (2012) analyzed the second of the three wave events and found evidence for a two-component hybrid-wave interpretation.

The applicability of imaging of the solar corona for analyzing structures or dynamics in the corona is hampered because the optical depth of the solar corona is in practice negligible. As a consequence, imaging telescopes necessarily measure an intensity resulting from an integration of the emission along the line of sight (LOS). For collisionally excited spectral lines such as those observed by EUV imagers, the intensity is given by an integral along the LOS of the electron density squared multiplied by a temperature response function,

$$I = \int \mathrm{d}s\, n_\mathrm{e}^2\, G(T, n_\mathrm{e}). \tag{1}$$

Therefore, only the *apparent* characteristics of EUV waves can be determined from imaging observations, and the deviation from the real ones is not known. Only with the launch of the twin STEREO spacecraft with identical, temporally synchronized EUV imagers has an observational assessment become possible. Comparing images taken by STEREO-A and STEREO-B of the 7 December 2007 event, Patsourakos *et al.* (2009) and Ma *et al.* (2009) found that in the early stages of the eruption the images of the EUV wave differed markedly, while at later times the wave appeared more alike in the two views. Furthermore, the wave appears to initially propagate in opposite directions in the two data sets. Ma *et al.* (2009) proposed these features to arise from the LOS projection effect on purely heuristic grounds.

In this work, we study the effect of projection and LOS integration on the morphology and kinematics of EUV waves, following the idea of Ma *et al.* (2009), but instead pursuing a quantitative modeling approach. To do this, we ran a three-dimensional magnetohydrodynamic (MHD) simulation of an erupting CME in an environment that mimicked the low corona and calculated the resulting emission measure of the event from different viewing angles. In addition to studying the effect of the viewing angle on the morphology and kinematics of the observed EUV wave event, we also compared our modeling results to earlier two-dimensional models of the EUV wave propagation. The article is organized as follows: in Section 2, we introduce the numerical model, and the results of the simulations are presented in Section 3. The results are discussed in Section 4.

2. The Model

We used a three-dimensional MHD model to which gravity is added as a body-force term in the ideal MHD equations. We have chosen the gravitational acceleration to be constant and assumed a homogeneous plasma temperature for the initial state. To set the corona initially in a state of static equilibrium, the plasma density decreases exponentially; we did not take the solar wind into account for this. We used a three-dimensional Cartesian simulation domain and assumed the solar surface to be flat, since the region of the corona where the eruption evolves in is relatively small. For the initial state magnetic field, we used the analytic equilibrium force-free model of Titov and Démoulin (1999), in which a semicircular flux rope carrying a toroidal current is embedded in a bipolar field produced by two subsurface magnetic charges and a subsurface line current. However, to produce an eruption, the parameters appearing in the Titov and Démoulin (1999) model were chosen such that an out-of-equilibrium configuration was obtained. This can be accomplished by reducing the strength of the subsurface current elements while keeping the parameters of the flux rope fixed. Specifically, we removed the line current completely in addition to reducing the strength of the magnetic charges from their equilibrium values.

The numerical method applied in the simulation is a conservative semi-discrete second-order finite volume scheme. The hyperbolic equations were solved by using the methods described by Kissmann, Pomoell, and Kley (2009). The induction equation was treated with a consistent constrained transport technique so that the magnetic field remained divergence-free up to machine precision (Kissmann and Pomoell, 2012). If the divergence is initially zero, it will remain so throughout the duration of the simulation. All boundary values were kept fixed throughout the simulation. For the bottom this implies a line-tying condition. For the other ones, the fixed boundary conditions do not allow a physically correct outflow of any large-scale structure like a CME. Therefore, the simulation results at the walls of the box represent physical conditions only in the steady state and the simulations had to be stopped before the eruption hit the walls (other than the bottom) of the simulation domain.

To mimic the coronal environment, the free parameters of the initial state of the model were chosen as follows: gravitational acceleration $g_\odot = 274\ \mathrm{m\,s^{-2}}$, density at the coronal base $\rho_0 = 1.67 \times 10^{-12}\ \mathrm{kg\,m^{-3}}$, and temperature at the coronal base $T_0 = 1$ MK. The length scale was chosen to be $l = 50$ Mm. These parameters give an approximate scale height of $H \approx 50$ Mm. We used the following values for the parameters describing the flux rope (see Figure 2 in Titov and Démoulin, 1999): major radius of the flux rope $R = 1.6l$, magnetic charges $q = 2.5 \times 10^{12}\ \mathrm{T\,m^2}$, which are located at a distance of $L = 0.3l$ from the axis of symmetry of the rope at depth $d = 0.8l$ below the photosphere. The radius of the circular cross-section of the flux rope was $a = 0.25l$, the ring current $I = 1.144 \cdot 10^{11}$ A, and the line-current I_0 was set to zero.

3. Results

Figure 1 presents an overview of the simulation run. Depicted is the density both in the yz-plane and in the xz-plane at four different times, $t = 50$, 100, 150, and 200 s. The yz-plane cuts the flux rope parallel to the rope axis and the xz-plane is the perpendicular cross section of the rope with the z-axis pointing upward away from the surface. Figure 2 presents the magnetic field strength in the two different planes. By looking at these two figures we can see that the leading edge of the eruption complex is characterized by a faint rising arc in the density plot. The flux rope is situated in the region below the arc. It can be seen in Figure 2 as a circular cross-section in the xz-plane and as an arc in the yx-plane, where the strength of the magnetic field increases. We interpret the dense region below the flux rope in the density plot (Figure 1) as the current sheet rising together with the entire structure. Just outside the footpoints of the flux rope there are two regions of dense plasma that move outward (toward the edges of the simulation box). They are pushed by the motion of the flux rope field lines near the surface as the eruption proceeds.

Figure 3 is a schematic picture of the set-up of this investigation. Shown are the five different cases studied in this paper. Small boxes indicate the position of the eruption on the surface of the Sun and the black lines show the orientation of the flux rope in each case. All cases are calculated from the same simulation, while a different viewing angle is selected to facilitate the interpretation in terms of LOS observation from the observatory. In each case the eruption is moving radially away from the surface. Cases are named with letters A – E and are shown in Figures 4 – 8.

Figures 4 – 8 show the snapshots of the normalized emission measure, calculated as

$$\mathrm{EM}(x_i, y_j) = \frac{\sum_{k=0}^{k_{\max}} \rho(x_i + k\Delta x, y_j + k\Delta y, k\Delta z)^2}{\sum_{k=0}^{k_{\max}} \rho_0 (k\Delta z)^2}, \tag{2}$$

where ρ is the density, ρ_0 is the density of the initial state with an exponentially decreasing density profile, Δx, Δy, and Δz are the step sizes in each direction. Note that $\Delta x/\Delta l$, $\Delta y/\Delta l$, and $\Delta z/\Delta l$, where $\Delta l = \sqrt{(\Delta x^2 + \Delta y^2 + \Delta z^2)}$, are the direction cosines of the LOS in the local coordinate system. The result becomes dimensionless when the emission measure is calculated as described above. We used the same scale from 0.5 to 2 for the emission measure in every figure to facilitate comparison. The emission measure exceeds 2 in the saturated regions. Different figures have slightly different maxima, but none of them exceeds 6.5.

Figure 4 (case A) shows the evolution of the emission measure of a CME that is erupting from the center of the disk toward the Earth and is viewed head-on (see Figure 3). In these snapshots we see a strong increase of the emission measure in the middle of the figure, which is staying more or less at the same position, while only the shape is evolving. When comparing this feature to Figure 1 we see that the stationary region of the strong emission measure is the dense current sheet. On both sides of the central structure there are two arc-like structures, which are growing and moving outward (direction 1 in Figure 4 (top panel)) from near the footpoints of the flux rope. These arcs are produced by the wave moving laterally as seen in the left panel of Figure 1. At time $t = 100$ s a fainter structure develops that connects the arcs. This fainter wave-like structure is moving along direction 2 marked in Figure 4 (top panel). Figure 1 shows that there is a fainter laterally traveling wave that also moves in this direction. However, the LOS integration of the dome, which is seen above the flux rope in Figure 1, contributes to the final emission measure in both cases as well. The features seen in the calculated emission measure arise from different structures at various altitudes in the CME.

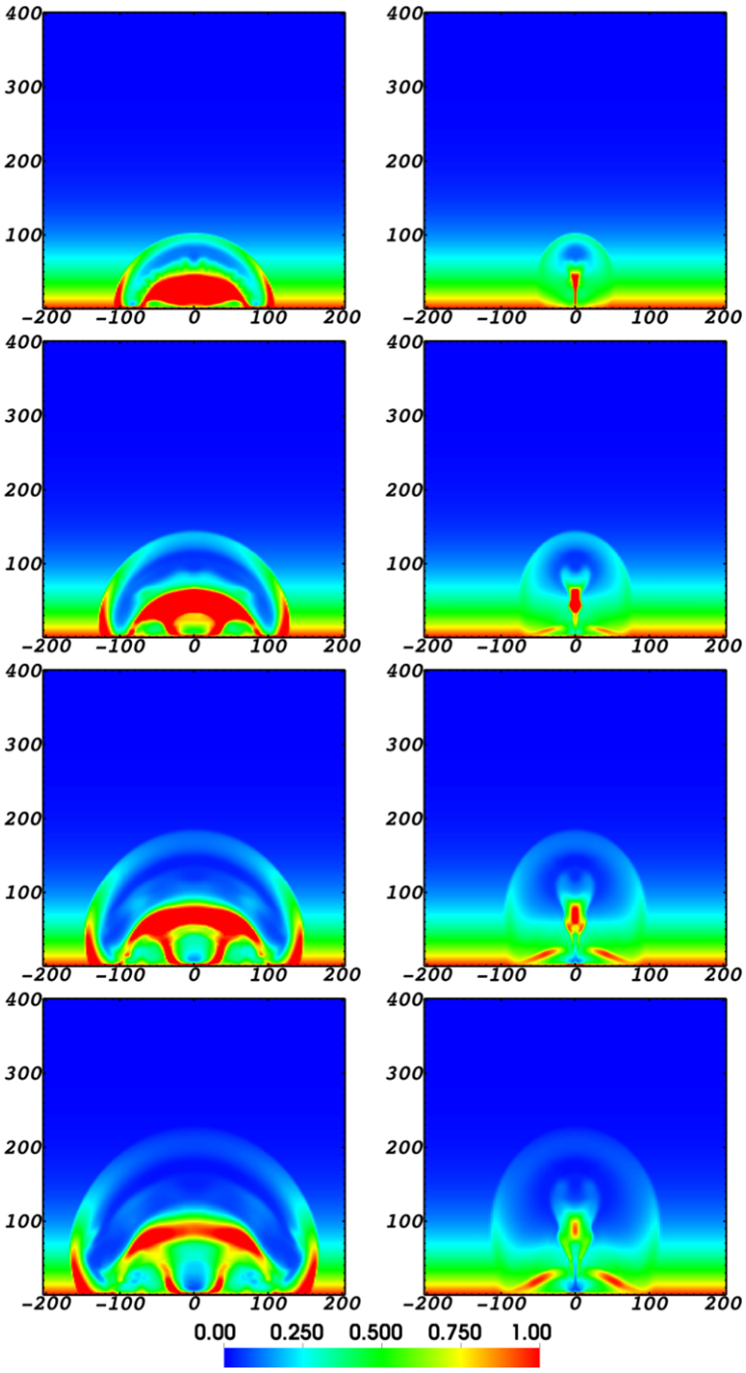

Figure 1 Density in the yz-plane (left panel) and the xz-plane (right panel) at four different times, starting from top $t = 50$, 100, 150 and 200 s. The yz-plane cuts the flux rope parallel to the rope axis and the xz-plane is the perpendicular cross section of the rope. The color-bar unit is $1.67 \cdot 10^{-12}$ kg m^{-3}.

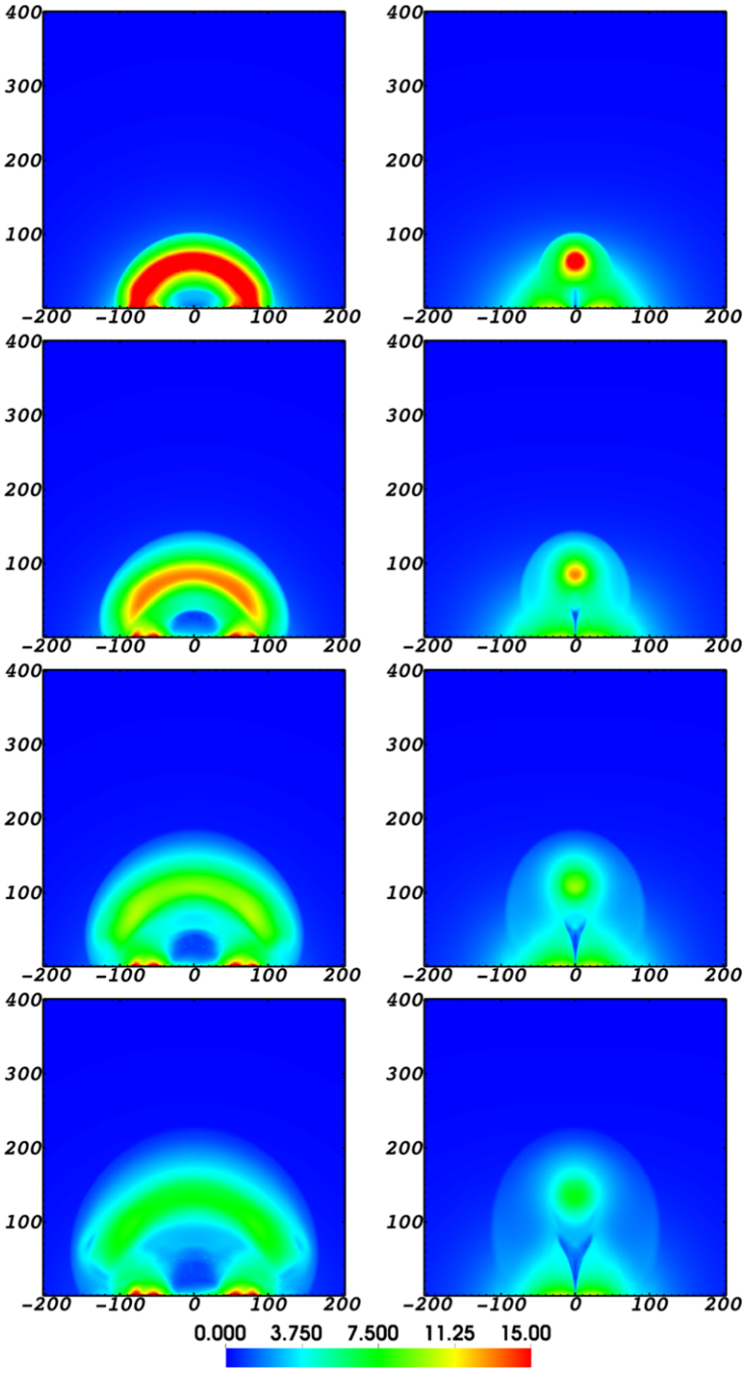

Figure 2 Magnetic field strength in the yz-plane (left panel) and the xz-plane (right panel) at four different times, starting from top $t = 50$, 100, 150 and 200 s. The yz-plane cuts the flux rope parallel to the rope and the xz-plane is the perpendicular cross section of the rope. The color-bar unit is 10^{-4} T.

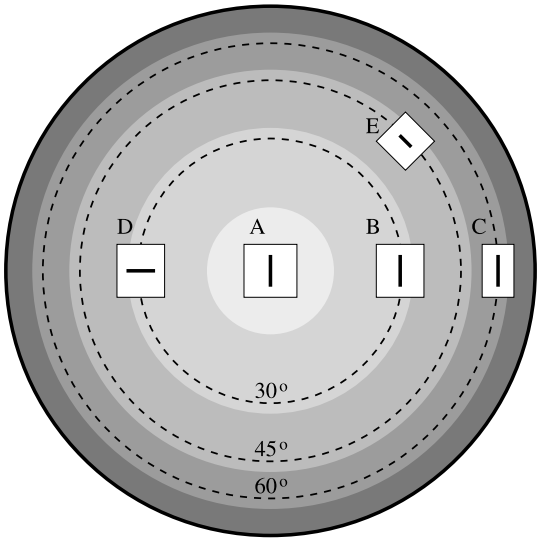

Figure 3 Schematic figure of the setup of this investigation. The small labeled boxes refer to different positions of the eruption on the surface of the Sun. The observer is in all cases on the radial line cutting through the center of the disk, which determines the direction of the LOS to the off-centered cases B – E.

The emission measure at time $t = 100$ s seen from different viewing directions is shown in Figures 5, 6, 7, and 8 (cases B – E, respectively). Cases B and C have the same orientation as the flux rope, but case C corresponds to a CME that takes place closer to the limb than in case B. In case D the CME is as close to the limb as in case B, but the orientation of the flux rope is tilted by 90°. In case E the orientation of the flux rope is tilted 45° compared to case A. Case E has been chosen to represent an off-equatorial CME that is seen from a different viewing angle than the CMEs located on the Equator. There is a faint structure that connects the arcs in cases B, C and E. This structure again comes from the LOS integration of the dome above the flux rope. In case E there is an S-shaped structure, which is another result from the dense plasma pushed by the flux rope close to the coronal base. This S-shaped structure is clearly separated from the structure that can be identified as the dome.

Case D (Figure 7) looks similar to case A (Figure 4). The main difference is that in case A the arcs are symmetric, but in case D the arc on the left-hand side is bigger than the one on the right. The central part of the strong emission measure seems to be slightly closer to the arc that is closer to the limb. In cases B, C, and E (Figures 5, 6, and 8) there is a faint structure from the dome that connects the arcs. This feature is not present in cases A (at time $t = 100$ s) and D. However, at time $t = 150$ s in case A, the dome has grown enough for the LOS integral to produce faint lines that connect both sides of the arcs.

Cases B and C look quite different even though in both the flux ropes have the same orientation. The shape of the structure is similar, but the arcs pushed by the field lines, lower down in the corona, look weaker in C than in B. The structure connecting the arcs is more sharp in B than in C. This is due to the different angle of the LOS integral through the dome. In case C the emission measure of the dense current sheet, which in every other case has a well-defined structure, seems to have two parts. In Figure 1 we see that the current sheet below the flux rope at time $t = 100$ s does not have a uniform shape.

In case A there are dimming regions, *i.e.*, regions where the emission measure has values below one. At the beginning (time $t = 50$ s) dimmings are stronger on the sides of the current sheet. During the eruption the dimmings increase closer to the footpoints. At time $t = 200$ s we see that the dimmings have developed into wing-like shapes. If the emission measure would have been studied along the perpendicular cross section of the flux rope,

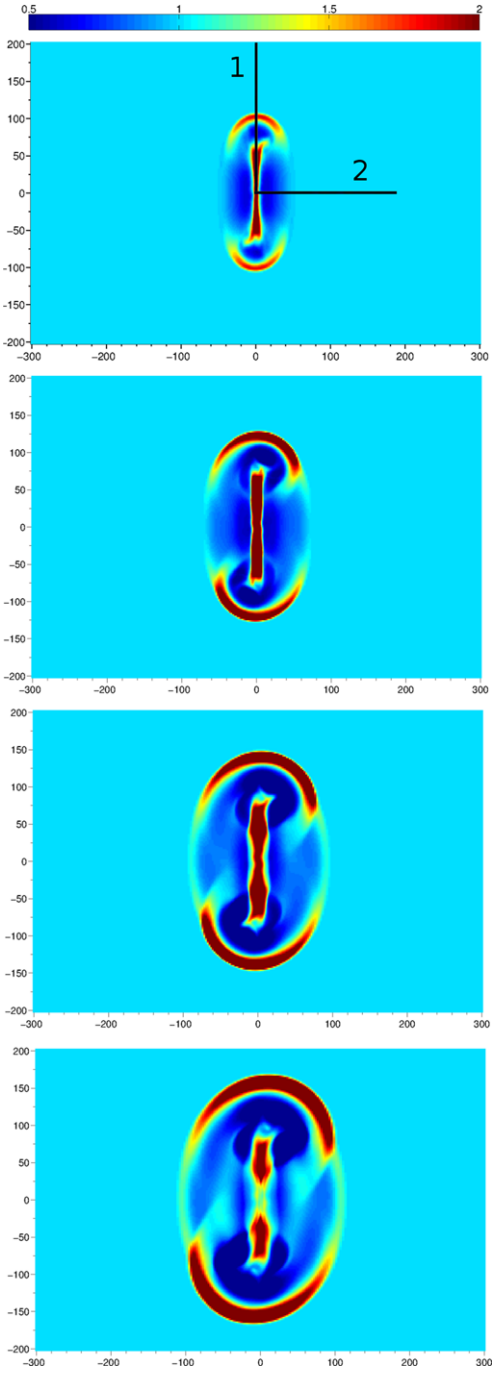

Figure 4 Case A, evolution of emission measure at four different times, $t = 50$, 100, 150, and 200 s. The horizontal and vertical axes are measured in Mm. The lines labeled as 1 and 2 in the top panel correspond to the directions in Figure 9.

we would have seen two separate dimming regions behind the emission measure increase. Between the two dimming regions the emission measure rises slightly above the ambient value. There are two dimming regions in this direction, but only one along the parallel cross

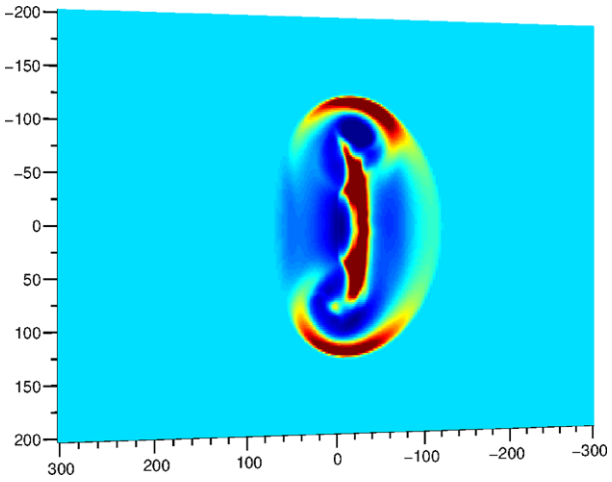

Figure 5 Case B, emission measure at time $t = 100$ s. Axes are measured in Mm. The scale of the color bar is the same as in Figure 4.

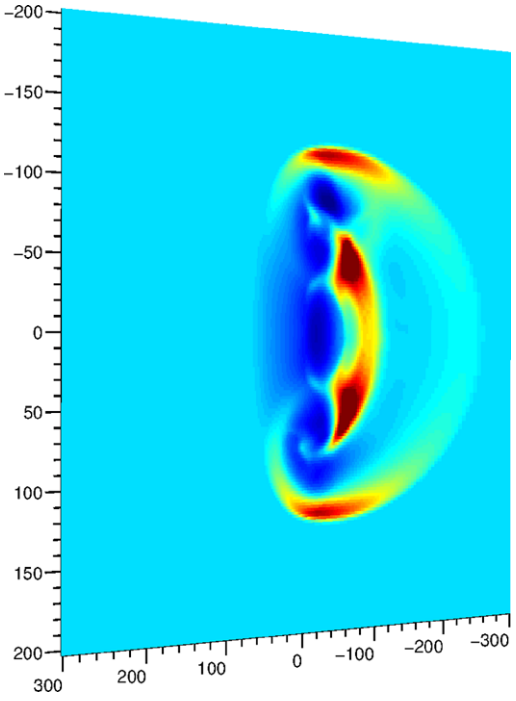

Figure 6 Case C, emission measure at time $t = 100$ s. Axes are measured in Mm. The scale of the color bar is the same as in Figure 4.

section. Comparing case A with cases B and C, we see that the closer the eruption is to the limb, the weaker the dimming on the limb side of the flux rope.

Figure 9 shows how the emission measure changes along the two lines drawn in Figure 4. The left panel corresponds to direction 1. The wave can be seen at the top of the figure as a red propagating front, below is the dimming region, and the thick dense area at the bottom of the figure is the current sheet. The speed of the wave front in this direction looks constant and is ~ 410 km s^{-1}. Direction 2 is shown in the right panel. The wave can be seen as a faint line, below we can also see the dimming region and part of the current sheet. In this

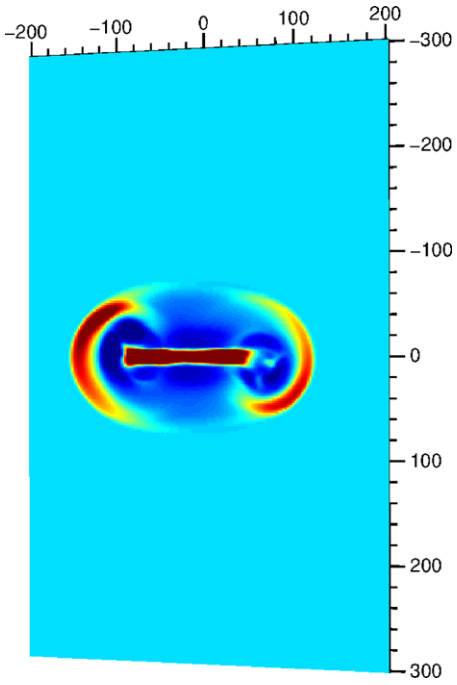

Figure 7 Case D, emission measure at time $t = 100$ s. Axes are measured in Mm. The scale of the color bar is the same as in Figure 4.

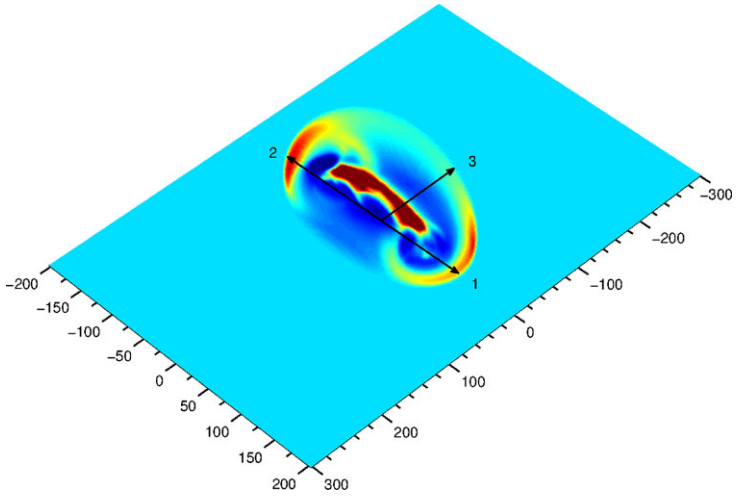

Figure 8 Case E, emission measure at time $t = 100$ s. Axes are measured in Mm. The scale of the color bar is the same as in Figure 4. Black arrows show the directions where the travel distance of the wave is calculated in Figure 11.

direction the speed of the propagating wave front is higher at the beginning; then the wave decelerates and, at the end, the speed looks to be more or less constant. The speed of the wave during the later phase is about 390 km s^{-1}.

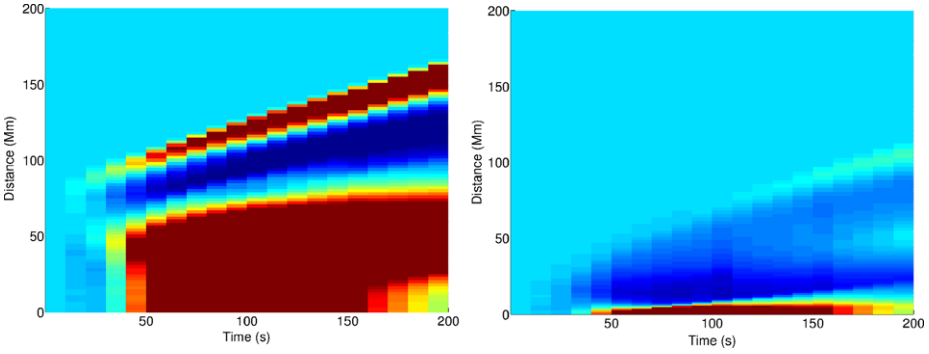

Figure 9 Evolution of the emission measure along the lines marked in Figure 4. Left panel shows direction 1 and right panel direction 2. Axes are measured in Mm. The scale of the color bar is the same as in Figure 4.

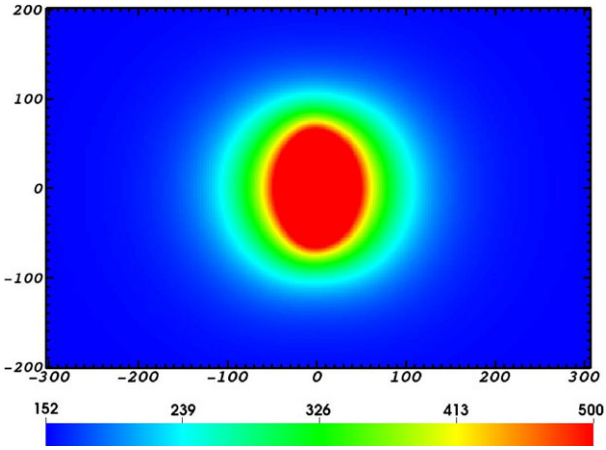

Figure 10 Magnetosonic speed at height 50 Mm. Axes are measured in Mm and the color-bar unit is 1 km s^{-1}

The waves we are interested in are traveling away from the flux rope perpendicular to the surrounding magnetic field. The velocity of the fast-mode MHD waves is then the magnetosonic speed, which is plotted in Figure 10. Comparing this figure with the kinematics of the wave in direction 2 (defined in Figure 4) as displayed in the right panel of Figure 9, the wave speed is observed to correspond well to the magnetosonic speed. First, the wave travels faster and later decelerates. If we now look at the magnetosonic speed in this direction, the speed is higher closer to the flux rope, but decreases to the ambient speed, which is 151 km s^{-1}. The same behavior can be seen in the wave moving along direction 2. However, the wave moving parallel to the flux rope (right panel in Figure 9) is faster than the local magnetosonic speed. We conclude that this wave is a shock wave propagating at super-magnetosonic speed.

In Figure 11 we show the time–distance plot of the rising dome (green) (calculated from Figure 1) and different wave-like features calculated from the emission measure figures in cases A (red) and E (light blue, blue, and orange). Case A corresponds to the wave traveling in direction 1 in Figure 4, which is the same case as the wave studied in the left panel of Figure 9. In case E we calculate the distance for three different waves traveling in the directions marked in Figure 8. The distance is calculated from the origin in every case. The dome rises faster than any of the other features. The feature along direction 3 in case E is the

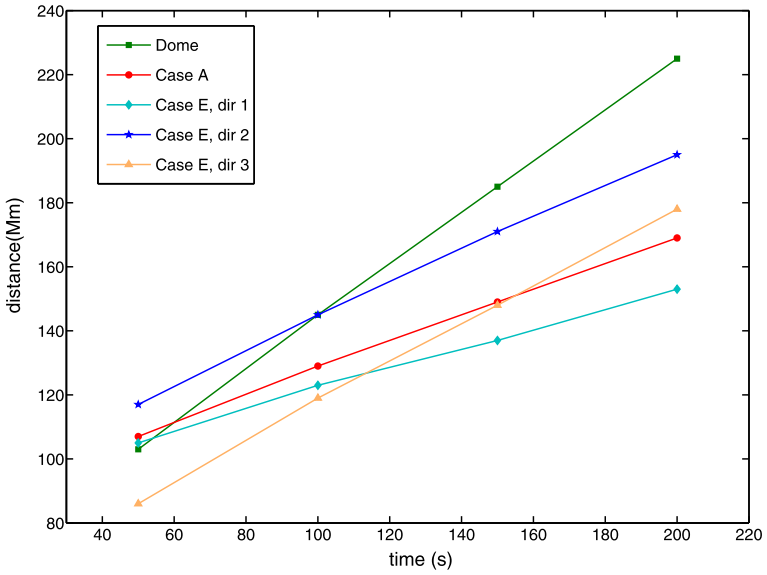

Figure 11 Time–distance plot of the rising dome (green) and wave-like features in cases A (red) and E (light blue, blue, and orange). Dir 1, 2, and 3 refer to the directions marked in Figure 8.

second-fastest, which is not surprising since it is the wave-like feature of the projected dome. In case E the wave moving in direction 1 (2) is moving toward (away from) the observer. The distance increases almost linearly in all the cases, which means that we can easily calculate the speeds. For the dome the actual speed is 810 $\mathrm{km\,s^{-1}}$. For case E directions 1, 2, and 3, the speeds are 320 $\mathrm{km\,s^{-1}}$, 520 $\mathrm{km\,s^{-1}}$, and 610 $\mathrm{km\,s^{-1}}$, respectively. The speed of the same feature, wave in case A and features along directions 1 and 2 in case E, highly depends on the viewing direction. In case A the speed is 410 $\mathrm{km\,s^{-1}}$, but for different viewing angles the speed can vary from 320 $\mathrm{km\,s^{-1}}$ to 520 $\mathrm{km\,s^{-1}}$, depending on whether the wave is moving toward or away from the observer.

4. Discussion and Conclusions

We have performed a three-dimensional MHD simulation of CME lift-off using the magnetic flux rope model described by Titov and Démoulin (1999). Our strategy was to view the same event from different viewing angles to facilitate the interpretation of EUV waves associated with the CME expansion in different directions. In several earlier studies (*e.g.*, Cohen *et al.*, 2009; Schmidt and Ofman, 2010 and Downs *et al.*, 2011) the global evolution of the EUV wave events has been investigated using three-dimensional MHD simulations using observational data as input. These studies have led to the conclusion that the EUV waves are hybrids of real and pseudo-waves. In this paper, we concentrated on the quantitative analysis of the local evolution of the waves during the early phases of a CME. Our calculations of the LOS-integrated emission measure do support the hybrid interpretation of EUV waves.

The time evolution of the emission measure shows arc-like increases moving outward that are pushed by the regions immediately above the footpoints of the flux rope. These features can be interpreted as EUV waves moving away from the eruption site. A comparison

of these features with the evolution of the density shown in Figure 1 indicates that the increases result from a real wave, which is pushed by the regions above the footpoints. This reinforces the true-wave nature of EUV waves. The density increase propagating ahead of the flux rope is the shock created by the eruption. This shocked plasma contributes to the LOS integral of the emission measure. The features seen in the emission measure result from a shock wave. Observationally, the true-wave interpretation has been supported by *e.g.* Patsourakos and Vourlidas (2009) and Kienreich *et al.* (2012). Patsourakos and Vourlidas (2009) studied the CME eruption that occurred on 13 February 2009, using data from the STEREO spacecraft. From the high cadence and quadrature *Sun Earth Connection Coronal and Heliospheric Investigation* (SECCHI) observations they were able to separate the CME structures from the signatures of the EUV wave. From these results they concluded that the EUV wave is a fast-mode MHD wave. Kienreich *et al.* (2012) conducted a study of three wave events that occurred on 27 January 2011, and found that the EUV waves were reflected from the southern polar coronal hole. The reflected waves obeyed the Huygens–Fresnel principle, indicating that the EUV transients were nonlinear large-amplitude MHD waves.

The speed of the EUV waves in our study varies from 320 $\mathrm{km\,s^{-1}}$ to 610 $\mathrm{km\,s^{-1}}$, depending on the viewing angle. These speeds are quite typical initial EUV wave speeds seen in high-cadence observations of *The Extreme Ultraviolet Imager* (EUVI) (Veronig, Temmer, and Vršnak, 2008). Our results suggest that the EUV waves have more or less constant speeds as a function of time, which is consistent with studies by *e.g.* Ma *et al.* (2009) and Kienreich, Temmer, and Veronig (2009), but inconsistent with Veronig, Temmer, and Vršnak (2008), whose analysis indicated decelerating waves. However, our study covers only the early stage of the CME and hence it is impossible to say whether the speed stays constant when the eruption proceeds further.

Our results show that the emission measure looks different depending on the viewing angle due to the projection effect. The same effect has been noted by Ma *et al.* (2009) in STEREO data. These authors compared the images taken by STEREO-A and STEREO-B of the 7 December 2007, event and found that during the early stages of the CME the EUV wave front seen by EUVI A seemed to be moving in an opposite direction to that seen by EUVI B, which they concluded to be due to a projection effect. The main difference between the results shown here and in Ma *et al.* (2009) is that we used the emission measure integrated along the LOS from a 3D MHD simulation, instead of interpreting STEREO data on heuristic grounds.

Clearly, the origin of the EUV wave observations is height-dependent and the strongest signals are seen from the footpoints of the CME as well as the current sheet. The dome of the CME contributes very little to the EUV wave emission in most viewing angles. However, in some cases the dome plays a significant role. These viewing angles result in a long LOS integral, tangential to the dome, which produces clearly visible features that can be interpreted as part of the EUV waves. This indicates that there is no consistent way to measure the speed of the EUV wave, since all features contributing to the wave are at different heights and thus the speed is measured dependent on the viewing angle. The leading edge of the dome in the plane of sky is visible as a faint part of the EUV wave.

A significant difference here compared to previous simulation works is that we performed a three-dimensional simulation. For example, Pomoell, Vainio, and Kissmann (2008) found in their two-dimensional simulation that behind the EUV wave front there is a clear depletion of the emission measure. In case of strong flux rope acceleration, they were able to see a secondary wave front propagating through the dimming behind the primary front. We found the same features when we looked perpendicularly to the cross section of the high-emission measure region at time $t = 200$ s. These depletions of the emission measure can be

interpreted as coronal dimmings observed after the lift-off of CMEs. Our three-dimensional study reveals that the coronal dimmings are propagating in all directions away from the erupting flux rope.

We conclude that SDO and STEREO data and simulation results needs to be interpreted carefully, keeping in mind the dependence on height of different features seen in EUV. This is important at least when measuring the speed of the EUV wave.

In summary, the simulation results showed EUV waves, reinforcing the true-wave nature of the leading edge of EUV waves. Behind the EUV wave front we identified coronal dimmings. There is no consistent way to measure the speed of the EUV wave from the emission measure because the origin of the EUV wave is height-dependent and hence varies with changing viewing directions. Our simulations study only the very beginning of the eruption, and consequently our results are not applicable for waves during the later phases of the eruption. Investigating the later phases of the CME would require a larger simulation box, for which the assumption of a flat surface is no longer valid and a spherical geometry should be employed. We leave this for a future study.

Acknowledgements The Academy of Finland is acknowledged for financial support (projects 133723, 138596, and 125481).

References

Chen, P.F.: 2011, Coronal mass ejections: models and their observational basis. *Living Rev. Solar Phys.* **8**, 1. http://www.livingreviews.org/lrsp-2011-1.

Cohen, O., Attrill, G.D.R., Manchester, W.B.IV, Wills-Davey, M.J.: 2009, Numerical simulation of an EUV coronal wave based on the 2009 February 13 CME event observed by STEREO. *Astrophys. J.* **705**, 587 – 602. doi:10.1088/0004-637X/705/1/587.

Dai, Y., Ding, M.D., Chen, P.F., Zhang, J.: 2012, Quadrature observations of wave and non-wave components and their decoupling in an extreme-ultraviolet wave event. *Astrophys. J.* **759**, 55. doi:10.1088/0004-637X/759/1/55.

Downs, C., Roussev, I.I., van der Holst, B., Lugaz, N., Sokolov, I.V., Gombosi, T.I.: 2011, Studying extreme ultraviolet wave transients with a digital laboratory: direct comparison of extreme ultraviolet wave observations to global magnetohydrodynamic simulations. *Astrophys. J.* **728**, 2. doi:10.1088/0004-637X/728/1/2.

Gallagher, P.T., Long, D.M.: 2011, Large-scale bright fronts in the solar corona: a review of "EIT waves". *Space Sci. Rev.* **158**, 365 – 396. doi:10.1007/s11214-010-9710-7.

Kienreich, I.W., Temmer, M., Veronig, A.M.: 2009, STEREO quadrature observations of the three-dimensional structure and driver of a global coronal wave. *Astrophys. J. Lett.* **703**, L118 – L122. doi:10.1088/0004-637X/703/2/L118.

Kienreich, I.W., Muhr, N., Veronig, A.M., Berghmans, D., De Groof, A., Temmer, M., Vršnak, B., Seaton, D.B.: 2012, Solar TErrestrial Relations Observatory-A (STEREO-A) and PRoject for On-Board Autonomy 2 (PROBA2) quadrature observations of reflections of three EUV waves from a coronal hole. *Solar Phys.* 138. doi:10.1007/s11207-012-0023-8.

Kissmann, R., Pomoell, J.: 2012, A semidiscrete finite volume constrained transport method on orthogonal curvilinear grids. *SIAM J. Sci. Comput.* **34**(2), 763 – 791. doi:10.1137/110834329.

Kissmann, R., Pomoell, J., Kley, W.: 2009, A central conservative scheme for general rectangular grids. *J. Comput. Phys.* **228**(6), 2119 – 2131. doi:10.1016/j.jcp.2008.11.030. http://www.sciencedirect.com/science/article/pii/S0021999108006207.

Ma, S., Wills-Davey, M.J., Lin, J., Chen, P.F., Attrill, G.D.R., Chen, H., Zhao, S., Li, Q., Golub, L.: 2009, A new view of coronal waves from STEREO. *Astrophys. J.* **707**, 503 – 509. doi:10.1088/0004-637X/707/1/503.

Moses, D., Clette, F., Delaboudinière, J.P., Artzner, G.E., Bougnet, M., Brunaud, J., Carabetian, C., Gabriel, A.H., Hochedez, J.F., Millier, F., Song, X.Y., Au, B., Dere, K.P., Howard, R.A., Kreplin, R., Michels, D.J., Defise, J.M., Jamar, C., Rochus, P., Chauvineau, J.P., Marioge, J.P., Catura, R.C., Lemen, J.R., Shing, L., Stern, R.A., Gurman, J.B., Neupert, W.M., Newmark, J., Thompson, B., Maucherat, A., Portier-Fozzani, F., Berghmans, D., Cugnon, P., van Dessel, E.L., Gabryl, J.R.: 1997, EIT observations of the extreme ultraviolet Sun. *Solar Phys.* **175**, 571 – 599. doi:10.1023/A:1004902913117.

Patsourakos, S., Vourlidas, A.: 2009, "Extreme ultraviolet waves" are waves: first quadrature observations of an extreme ultraviolet wave from STEREO. *Astrophys. J. Lett.* **700**, L182 – L186. doi:10.1088/0004-637X/700/2/L182.

Patsourakos, S., Vourlidas, A.: 2012, On the nature and genesis of EUV waves: a synthesis of observations from SOHO, STEREO, SDO, and Hinode. *Solar Phys.* **281**, 187 – 222. doi:10.1007/s11207-012-9988-6 (Invited Review).

Patsourakos, S., Vourlidas, A., Wang, Y.M., Stenborg, G., Thernisien, A.: 2009, What is the nature of EUV waves? First STEREO 3D observations and comparison with theoretical models. *Solar Phys.* **259**, 49 – 71. doi:10.1007/s11207-009-9386-x.

Pomoell, J., Vainio, R., Kissmann, R.: 2008, MHD modeling of coronal large-amplitude waves related to CME lift-off. *Solar Phys.* **253**, 249 – 261. doi:10.1007/s11207-008-9186-8.

Schmidt, J.M., Ofman, L.: 2010, Global simulation of an Extreme Ultraviolet Imaging telescope wave. *Astrophys. J.* **713**, 1008 – 1015. doi:10.1088/0004-637X/713/2/1008.

Thompson, B.J., Plunkett, S.P., Gurman, J.B., Newmark, J.S., St. Cyr, O.C., Michels, D.J.: 1998, SOHO/EIT observations of an Earth-directed coronal mass ejection on May 12, 1997. *Geophys. Res. Lett.* **25**, 2465 – 2468. doi:10.1029/98GL50429.

Thompson, B.J., Gurman, J.B., Neupert, W.M., Newmark, J.S., Delaboudinière, J.P., St. Cyr, O.C., Stezelberger, S., Dere, K.P., Howard, R.A., Michels, D.J.: 1999, SOHO/EIT observations of the 7 April 1997 coronal transient: possible evidence of coronal Moreton waves. *Astrophys. J. Lett.* **517**, L151 – L154. doi:10.1086/312030.

Titov, V.S., Démoulin, P.: 1999, Basic topology of twisted magnetic configurations in solar flares. *Astron. Astrophys.* **351**, 707 – 720.

Uchida, Y.: 1968, Propagation of hydromagnetic disturbances in the solar corona and Moreton's wave phenomenon. *Solar Phys.* **4**, 30 – 44. doi:10.1007/BF00146996.

Veronig, A.M., Temmer, M., Vršnak, B.: 2008, High-cadence observations of a global coronal wave by STEREO EUVI. *Astrophys. J. Lett.* **681**, L113 – L116. doi:10.1086/590493.

Vršnak, B., Cliver, E.W.: 2008, Origin of coronal shock waves. Invited review. *Solar Phys.* **253**, 215 – 235. doi:10.1007/s11207-008-9241-5.

Warmuth, A.: 2007, Large-scale waves and shocks in the solar corona. In: Klein, K.L., MacKinnon, A.L. (eds.) *Lecture Notes in Physics* **725**, Springer, Berlin, 107.

Warmuth, A.: 2010, Large-scale waves in the solar corona: the continuing debate. *Adv. Space Res.* **45**, 527 – 536. doi:10.1016/j.asr.2009.08.022.

Warmuth, A.: 2011, Globally propagating waves in the solar corona. *Plasma Phys. Control. Fusion* **53**(12), 124023. doi:10.1088/0741-3335/53/12/124023.

Wills-Davey, M.J., Attrill, G.D.R.: 2009, EIT waves: a changing understanding over a solar cycle. *Space Sci. Rev.* **149**, 325 – 353. doi:10.1007/s11214-009-9612-8.

Zhukov, A.N.: 2011, EIT wave observations and modeling in the STEREO era. *J. Atmos. Solar-Terr. Phys.* **73**, 1096 – 1116. doi:10.1016/j.jastp.2010.11.030.